A&A 620, A57 (2018)
https://doi.org/10.1051/0004-6361/201832976

Astronomy & Astrophysics

Ultrahigh-resolution model of a breakout CME embedded in the solar wind*

S. Hosteaux[1], E. Chané[1], B. Decraemer[2,1], D.-C. Talpeanu[1,2], and S. Poedts[1]

[1] Centre for mathematical Plasma Astrophysics (CmPA), Department of Mathematics, KU Leuven, Celestijnenlaan 200B, 3001 Leuven, Belgium
e-mail: skralan.hosteaux@kuleuven.be
[2] Royal Observatory of Belgium (ROB), Ringlaan 3, 1180 Brussels, Belgium

Received 7 March 2018 / Accepted 12 September 2018

ABSTRACT

Aims. We investigate the effect of a background solar wind on breakout coronal mass ejections, in particular, the effect on the different current sheets and the flux rope formation process.
Methods. We obtained numerical simulation results by solving the magnetohydrodynamics equations on a 2.5D (axisymmetric) stretched grid. Ultrahigh spatial resolution is obtained by applying a solution adaptive mesh refinement scheme by increasing the grid resolution in regions of high electrical current, that is, by focussing on the maximum resolution of the current sheets that are forming. All simulations were performed using the same initial base grid and numerical schemes; we only varied the refinement level.
Results. A background wind that causes a surrounding helmet streamer has been proven to have a substantial effect on the current sheets that are forming and thus on the dynamics and topology of the breakout release process. Two distinct ejections occur: first, the top of the helmet streamer detaches, and then the central arcade is pinched off behind the top of the helmet streamer. This is different from the breakout scenario that does not take the solar wind into account, where only the central arcade is involved in the eruption. In the new ultrahigh-resolution simulations, small-scale structures are formed in the lateral current sheets, which later merge with the helmet streamer or reconnect with the solar surface. We find that magnetic reconnections that occur at the lateral breakout current sheets deliver the major kinetic energy contribution to the eruption and not the reconnection at the so-called flare current sheet, as was seen in the case without background solar wind.

Key words. magnetohydrodynamics (MHD) – Sun: coronal mass ejections (CMEs) – magnetic reconnection

1. Introduction

Coronal mass ejections (CMEs) are very violent outbreaks of magnetic field and plasma originating from the solar corona. Their occurrence rate ranges from one ejection per week during solar minimum to 2–3 ejections per day during solar maximum, of which approximately 3.5% are directed toward Earth (Gopalswamy 2004). In addition to the intriguing auroras at higher latitudes, the interaction between the Earth's intrinsic magnetic field and an impacting CME can have several negative space weather impacts (Singh et al. 2010; Riley et al. 2018). Magnetic storms resulting from this interaction can disturb or even interrupt communication and navigation systems, induce direct current peaks in power supplies, damage satellites, and harm astronauts. CME velocities usually vary between 400–500 km s^{-1}, although speeds of over 2000 km s^{-1} can also occur. Insight into the triggering mechanism(s) and the initiation and propagation characteristics of CMEs is of vital importance for understanding space weather phenomena and for predicting them. In this regard, numerical magnetohydrodynamic (MHD) modeling has proven to be an effective tool for providing the global picture of the Sun-Earth interaction, which starts with the initiation of a CME in the lower atmosphere of the Sun.

There is, however, no consensus on what the precise triggering mechanism of a CME is. Several types of models exist, and they mostly agree that the main energy input for CMEs must come from the coronal magnetic field, where it has first been stored. One possible method for accumulating free magnetic energy is believed to be the shearing of magnetic fields as a result of photospheric plasma motions (Steinolfson 1991). It has been observed that horizontal motions in the photosphere are involved in solar eruptions, and numerical models have also been developed that achieve an eruption that starts from only a closed magnetic arcade and imposes shearing motions at the foot points of the arcade, which creates first a magnetic flux rope that is expelled in a later phase (Jacobs et al. 2005, 2006; van der Holst et al. 2007; Zuccarello et al. 2009). CMEs that are initiated in this manner are called breakout CMEs (Antiochos 1998; Antiochos et al. 1999). The shearing motions at the footpoints are not a necessary factor in the breakout model, however, only a possible mechanism for stressing the fields. For example, magnetic flux emergence is another method by which CME eruptions are achieved with the breakout model (Leake et al. 2014). The only requirement is that the field is stressed slowly. In the eruption phase, the previously stored magnetic energy is converted into kinetic energy via magnetic reconnection that occurs in different thin electric current sheets. The parameters of the reconnecting current sheet are determined by global system conditions and conservation laws such as mass and flux conservation. In numerical simulations, instabilities such as the

* The movies associated to Figs. 3 and A.1 are available at https://www.aanda.org

tearing mode instability induce the formation of small-scale magnetic structures in order to introduce new scales to the system to satisfy the global conditions as well as the conservation laws (Janvier 2017; Edmondson et al. 2010). Such plasmoids, called magnetic islands in 2D, are encountered in both laboratory (Smolyakov et al. 1995; Zhao et al. 2015) and space plasmas (Chian & Muñoz 2011; Eriksson et al. 2014). These magnetic islands are similar to the magnetic cloud of a CME, but much smaller in size. They are dynamically shaped and often appear in groups. Furthermore, they can merge or split, depending on the conditions, and play a role in particle acceleration when particles are trapped inside the magnetic islands (Khabarova et al. 2015, 2016).

Studies by van der Holst et al. (2007) and others demonstrated that the background wind, which forms a helmet streamer around the initial triple-arcade structure, substantially affects the different magnetic reconnection phenomena involved in the formation of the magnetic flux rope and its subsequent release. When numerical simulations are performed, a very high spatial resolution is necessary to resolve the small-scale structures that develop in the current sheets. An adaptive mesh refinement (AMR) scheme that dynamically refines the grid at the location of the current sheets was used by Karpen et al. (2012) and also in a follow-up paper by Guidoni et al. (2016), in which the authors discussed the intricate details of the dynamics of these magnetic islands.

This paper presents an important advancement by employing solution-dependent AMR to perform ultrahigh-resolution simulations of a breakout CME that expands in a surrounding helmet streamer as a result of a background solar wind. We observe and discuss the effects of including a background wind on the breakout scenario and the early evolution of the breakout CME, focussing on the dynamics and the role of the small-scale magnetic structures that form in the different (breakout and flaring) current sheets.

The next section briefly describes the numerical model and methods we used. The model set-up of the initial triple-arcade structure that is embedded in a helmet streamer is then presented together with a description of the driving mechanism. The results of the different ultrahigh-resolution simulations are presented, analysed, and discussed in the next section. The final section contains our conclusions.

2. Numerical method and solution-dependent AMR strategy

The simulations were performed by numerically solving the MHD equations on a spherical logarithmically stretched grid using MPI-AMRVAC (Porth et al. 2014; Xia et al. 2018) in 2.5D, which means that all three components (r-, θ-, and ϕ-components in the spherical coordinates used here) of the vectors are included, but the simulations are solved on a 2D mesh, as the whole solution is assumed to be axisymmetric and thus independent of the ϕ coordinate. In reality, the solar magnetic field has a fully 3D configuration, but 2.5D simulations have been shown to yield very similar results (height-time curves, shocks, spread angles, etc.) to their fully 3D counterparts while being less computationally intensive by two orders of magnitude (Jacobs et al. 2007). The computational domain in our setup spans $[1, 30]\,R_\odot$ in the radial (r) direction and $[0, \pi]$ radians in the latitudinal (θ) direction.

To achieve the highest possible resolution, an AMR protocol was used with up to seven grid levels, meaning that an additional six levels of refinement were added to the base grid, which yielded a resolution up to $2^6 = 64$ times higher when and where needed. The AMR scheme is block-based, which means that the domain is divided into blocks that contain a number of cells, and if a refinement condition is met at a cell inside a certain block, all the cells in that block are refined. The choice of where the mesh is to be refined or coarsened is based on the following parameter, taken from Karpen et al. (2012):

$$c \equiv \frac{|\iint_S \nabla \times \boldsymbol{B} \cdot \mathrm{d}\boldsymbol{a}|}{\oint |\boldsymbol{B} \cdot \mathrm{d}\boldsymbol{l}|} = \frac{|\oint_C \boldsymbol{B} \cdot \mathrm{d}\boldsymbol{l}|}{\oint_C |\boldsymbol{B} \cdot \mathrm{d}\boldsymbol{l}|} = \frac{|\sum_{n=1}^{4} B_{t,n}\, l_n|}{\sum_{n=1}^{4} |B_{t,n} l_n|}. \quad (1)$$

This refinement parameter c corresponds to a dimensionless measure that enables identifying current-carrying structures, that is, current sheets, where magnetic reconnection can occur so that these need to be resolved as they are crucial for the breakout model. The notation $B_{t,n}$ corresponds to the tangential component of the magnetic field along the nth segment l_n of contour C, with S the surface bounded by the contour. Thus the equation states that c is the ratio of the net electric current magnitude passing through surface S and the sum of the absolute value of all electric current contributions to the contour.

When a strong current-carrying structure is present in a certain grid block, the value of c is close to one. In the AMR strategy applied here, when $c > c_1$, the block is refined, and if $c < c_2$, it is coarsened back to a lower level. We here chose $c_1 = 0.02$ and $c_2 = 0.01$, as these threshold values were found to be the optimal values for refining the current-carrying structures: they yielded very localized grid adaptations and thus kept the total amount of grid points (and thus the CPU time demands) within reasonable bounds. This method with these thresholds on the parameter c ensures that the grid dynamically refines to the highest refinement allowed at the location of the current sheets. At the lowest level, the (initial base) grid cells are $0.0105\,R_\odot$ radially and $0.012\,R_\odot$ latitudinally at the solar base, while at the highest refinement level, they extend $1.625\times10^{-4}\,R_\odot$ radially and $1.875 \times 10^{-4}\,R_\odot$ latitudinally. The effective resolution of the simulation with seven grid levels yields 3.67×10^8 (effective) grid cells, that is, we would have this number of grid cells if the whole computational domain had the highest resolution. However, as the mesh is solution adaptive, the resolution only increases where needed. As a result, the highest number of cells at any point during the run is 3.02×10^6. Since the background solar wind, which is assumed to be in quiet-Sun condition, has a heliospheric current sheet (HCS) on the equatorial plane spanning the whole computational domain, this HCS would also be resolved as soon as the AMR simulation starts. Because this would significantly increase the computational cost and our interest is only in the eruption, an additional time-dependent condition on the refinement was implemented that limited the refinement at a given radial distance up to a few hours before the CME reaches this location. This condition limits the AMR scheme to a region where $r < 3\,R_\odot$ if $t < 14$ h, while if $14\,\mathrm{h} \leq t < 20$ h, the refinement is limited to $7\,R_\odot$, and if $20\,\mathrm{h} \leq t < 24$ h, there is no refinement beyond $11\,R_\odot$. No radial restriction is placed on the refinement after 24 h.

3. Breakout CME setup

To achieve a fast-slow-fast bimodal wind structure, it is necessary to use an additional heating and momentum deposition. In addition to the gravitational force, our model therefore includes a radial and latitude-dependent empirical heating source term that

is added to the energy equation. This additional term takes the form (Manchester et al. 2004)

$$Q = \rho q_0 (T_0 - T) \exp\left[-\frac{(r-1)^2}{\sigma_0^2}\right], \tag{2}$$

where ρ is the mass density, q_0 the volumetric heating amplitude, T_0 the target temperature, T the plasma temperature, and σ_0 the heating scale height. T_0 is 1.5×10^6 K equator-ward from a certain critical angle θ_0, and it is 2.63×10^6 K pole-ward from this angle. The heating scale height σ_0 is 4.5 equator-ward from the same critical angle and $4.5\,[2 - \sin^2\theta/\sin^2\theta_0]$ poleward. For $r \leq 7\,R_\odot$ the critical angle is given by $\sin^2\theta = \sin^2(17.5°) + \cos^2(17.5°)(r/R_\odot - 1)/8$, while for $7\,R_\odot < r$, this changes to $\sin^2(\theta_0) = \sin^2(61.5°) + \cos^2(61.5°)(r/R_\odot - 7)/40$. Last, q_0 is given a value of 10^{-13} J s^{-1} K^{-1}.

At the inner boundary, the number density was fixed at the solar base to 10^8 cm^{-3} and the temperature to 1.5×10^6 K. The longitudinal velocity component v_ϕ was set, in addition to the shearing term (discussed below), to impose the differential rotation of the Sun. The differential rotation has little influence on the evolution of the eruption, however, since the rotation speed is considerably lower than the shearing speed at the footpoints. On the other hand, v_θ was set to zero at the inner boundary, while v_r was set to zero in the ghost cells. In addition, $r^2 B_r$ was fixed at the inner boundary in order to obtain a dipole field at the boundary, and the triple-arcade term was added near the equator (see below). Moreover, $r^3 B_\theta$ and B_ϕ were continuous, meaning that their value was copied from the closest inner cell.

At the outer boundary, $r^2\rho$, $r^2 v_r$, v_θ, $r v_\phi$, $r^2 B_r$, B_θ, $r B_\phi$, and T are continuous. For the simulations discussed in the present paper, the total variation diminishing Lax-Friedrichs scheme was used in combination with the minmod slope limiter.

When the background solar wind is taken into account, a more realistic but also more complicated situation arises than was described in Karpen et al. (2012). The background magnetic field was constructed with a magnetic dipole field with a magnitude of 2.2 G at the poles and by adding an additional quadripole term to the magnetic field to obtain a superposed triple-arcade structure near the equator. This additional vector potential term, taken from van der Holst et al. (2007), has the form

$$A_\phi = \frac{A_0}{r^4 \sin\theta} \cos^2\left(\frac{\pi\lambda}{2\Delta\theta}\right), \tag{3}$$

with $\lambda = \pi/2 - \theta$ corresponding to the solar latitude, and $A_0 = -7.3$ G. This additional term was only added to the dipole field when $|\lambda| < 0.5$. The initial configuration is shown in Fig. 1. The relaxed state shown here is reached at about 160 h after initializing the wind. The left panel shows the velocity distribution of the wind, and the right panel shows the triple-arcade magnetic structure and the overlying helmet streamer. This steady-state equilibrium acts as the initial state on which the shearing motions are applied to initiate a breakout CME.

The shearing of the inner arcade is obtained by imposing a time-dependent inner boundary condition on the longitudinal component of v,

$$v_\phi^{\text{shear}} = v_0 (\lambda^2 - \Delta\theta^2)^2 \sin\lambda \sin(\pi t/\Delta t), \tag{4}$$

if $|\lambda| < 0.12$. The shearing region falls well within the central arcade foot-points, while outside this region, $v_\phi^{\text{shear}} = 0$. The amplitude v_0 was chosen such that v_ϕ reached a maximum speed of ± 20 km s^{-1}, which is two orders of magnitude smaller than the Alfvén speed in the corona, so that the evolution of the system responding to the shearing flows can be considered as quasi-static. The shearing duration Δt was set to 27 h. Equation (4) provides a smooth ramp-up to the maximum shearing speed of ± 20 km s^{-1} during $0 \leqslant t \leqslant 13.5$ and subsequently returns to zero until t reaches 27 h.

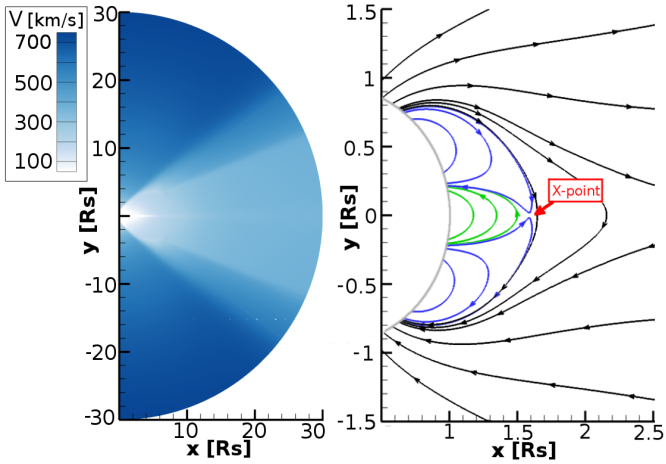

Fig. 1. Relaxed state of the solar wind, reached 160 h after initializing the wind. The *left panel* displays the speed of the background wind, and the *right panel* shows the selected magnetic field lines. The triple-arcade structure consists of the green and blue field lines, where the green lines represent the central arcade and the blue lines represent the side arcades. The background magnetic field is depicted by the black field lines.

4. Simulation results

4.1. Global eruption

The shearing motion applied at the base of the central arcade pumps magnetic energy into the central arcade by increasing the B_ϕ field component. In this way, an imbalance is introduced between magnetic pressure and magnetic tension. This leads to an expansion of the central arcade and causes it to push against the overlying magnetic field. As a result, the X-point between the arcade and the overlying field is flattened sufficiently for magnetic reconnection to occur. This opens the overlying magnetic field and thus facilitates the upward rise of the central arcade, which in turn increases the reconnection rate and results in a positive feedback process. The magnetic reconnection between the central arcade and the overlying field is known as the breakout reconnection, which in our model results in a total disconnection and ejection of the top of the helmet streamer. As the process progresses, the sides of the expanding arcade are stretched and converge, leading to another magnetic reconnection event, but this time below the eruption; this is called flare reconnection. As a consequence, the portion of the central arcade that reconnects to form a disconnected flux rope is ejected. This eruption process is very similar to previous studies regarding axisymmetric breakout scenarios that included a background solar wind (van der Holst et al. 2005, 2007; Lynch et al. 2011; Allred & MacNeice 2015).

Figure 2 shows the intricate details of the dynamical evolution of the breakout CME, in particular, the magnetic reconnection events involved in it, simulated with six additional levels of solution-dependent AMR. The upper left panel shows that

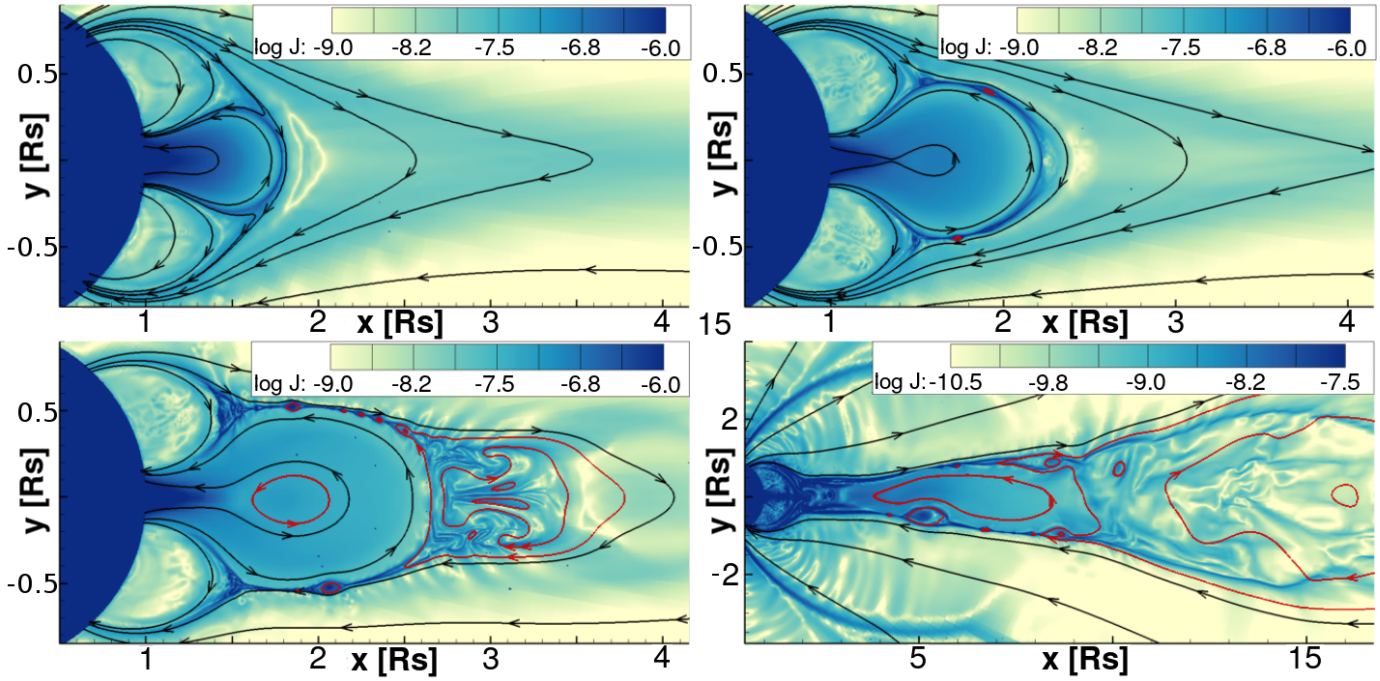

Fig. 2. Magnetic field lines and current density magnitude (A m^{-2}) of the seven-level simulation at different times after shearing starts. The *upper panels* are at $t = 15$ h and $t = 17.16$ h from *left* to *right*, the *bottom panels* are at $t = 20$ h and at $t = 30$ h from *left* to *right*. Closed magnetic structures are shown as red lines. The temporal evolution of the current density can be found in Fig. A.1.

15 h after the start of the foot point shearing phase, the central arcade has expanded substantially and consequently started pushing against the overlying magnetic field of the surrounding helmet streamer. As the central arcade rises even higher, it also pushes more strongly against the side arcades. Because of this, and because the overlying helmet streamer pushes back from the outside, the tops of the two lateral arcades become narrower. After 17 h, the stretching of the original single x-point into an elongated current sheet thus generated thin current sheets at the top of each side arcade at approximately $[1.9, 0.4]\,R_\odot$ and $[1.9, -0.4]\,R_\odot$ (which is a generic deformation whenever spline lines are separated by applied stresses, see, e.g., Janvier 2017). At this point, that is, after 17 h of shearing, the first small-scale magnetic structures can also be distinguished in these current sheets at the flanks, which are marked by the small red dots in the upper right panel of Fig. 2, signifying the onset of fast reconnection. These are small magnetic islands that emerge as in this figure (also in the subsequent panels) all closed magnetic field lines are shown in red. The breakout reconnection processes that occur at the sides of the rising arcade ultimately lead to the complete detachment of the helmet streamer. The same (upper right) panel of Fig. 2 shows that as the central arcade has risen, its base has become elongated enough (a current sheet has formed in which the current density has increased enough) for magnetic reconnection to set in. As a result of this flare reconnection, the central arcade is pinched off and is ejected behind the already detached top of the helmet streamer. At that moment, that is, 20 h after shearing commenced, many magnetic islands have formed in the current sheets in addition to the two large completely detached structures, as can be observed in the lower left panel of Fig. 2. The magnetic islands are clearly visible as closed field lines in the current sheets shown in red. These magnetic islands migrate either toward the detached helmet streamer, where they cause further turmoil in the already heavily disturbed detached helmet streamer, or toward the solar surface, where they reconnect with the side arcades and return magnetic energy to the remaining arcade system. To fully appreciate the complexity of the dynamics of the magnetic islands and the grid refinement evolution, we refer to the online movie. Finally, the lower right panel of Fig. 2 displays a snapshot of the situation 30 h after the start of the foot point shearing. At this point, new magnetic islands are still being produced in the lateral current sheets. Moreover, the detached top of the helmet streamer has greatly increased in size, whereas the pinched-off central arcade has become flattened or elongated as a result of the solar wind, which pushes from the sides. The central arcade has become somewhat misshapen as a result of some growing magnetic islands in the lateral current sheets.

Figure 3 and the accompanying online movie follow the detailed evolution of the breakout current sheet at the apex of the central arcade, from the moment it is formed to after the detachment of the top of the helmet streamer. The figure shows six snapshots of the current density together with the magnetic field lines, zooming out as the structure grows. In the first two panels in the upper row, the central arcade rises, which leads to the formation of the breakout current sheet as the field lines of opposite polarity converge toward each other and the X-point is flattened, forming the current sheet. In the second (middle) panel of the top row, the breakout current sheet has split into two lateral current sheets, which still transfer magnetic flux out of the way of the erupting structure and disconnect the top of the helmet streamer. The formation of the first magnetic islands can already be observed at both ends of the current sheet at approximately $[1.9, 0.4]\,R_\odot$ and $[1.9, -0.4]\,R_\odot$. Later, some magnetic islands move toward the apex of the arcade, that is, the center of the breakout current sheet, thus again widening the X-point. Because of the symmetric setup we study here, this ultimately leads to a current sheet perpendicular to the breakout current sheet, as indicated by the red arrow in the third panel at about $[2.6, 0.0]\,R_\odot$. At this location, the tips of the X-point reconnect,

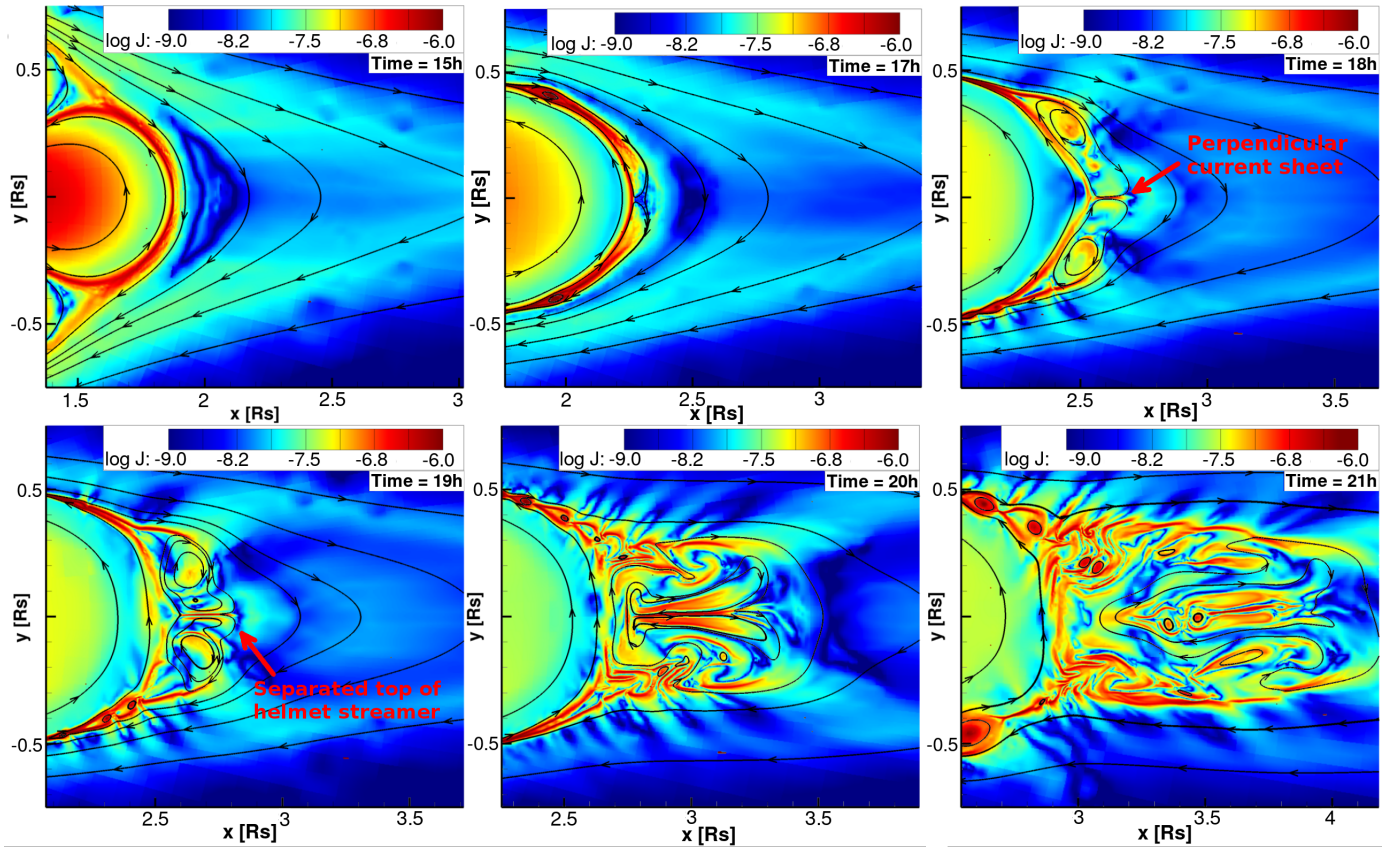

Fig. 3. Magnetic field lines and current density magnitude (A m^{-2}) of the seven-level simulation following the breakout current sheet at different times after shearing starts. The *upper panels* are at $t = 15.5$ h, $t = 17.33$ h and $t = 18.67$ h from *left* to *right*, the *bottom panels* are at $t = 19$ h, $t = 20$ h and at $t = 21$ h from *left* to *right*. The temporal evolution is also available as a movie online.

creating a single separate flux rope from the top of the helmet streamer; this is shown in the first (left) panel in the bottom row. Inside the separated flux rope, the magnetic islands continuously converge, while at the same time, more magnetic islands in the lateral current sheets are generated. As stated in the previous paragraph, some of these islands move toward the side arcades, while some move toward the detached top of the helmet streamer where they merge with the separated flux rope. The middle panel in the bottom row shows that the shape and internal dynamics and topology of the separated helmet streamer top are greatly affected by the merging with the magnetic islands. Finally, in the last (right) panel of the bottom row of Fig. 3, two small magnetic islands develop in the narrow current sheet perpendicular to the arcade apex, at approximately $[3.5, 0.0]\,R_\odot$, indicating the importance of the AMR scheme for resolving the internal quasi-turbulent reconnection within larger-scale flux structures.

As the central arcade detaches, the flare current sheet is formed below the CME, where small magnetic islands form as well, as the more detailed Fig. 4 shows. The upper panel of this figure shows the magnetic field strength, while the lower panel displays the magnitude of the electric current density, both at 36 h after the start of the foot point shearing. The formation of multiple islands in quick succession is clearly visible. Such magnetic island formation was also present in the ultrahigh-resolution simulations of Karpen et al. (2012), and in a subsequent paper, Guidoni et al. (2016) even focussed on the formation and dynamics of these islands. The outcome in our ultrahigh simulations, however, is very different from what is seen if high-resolution runs are made without taking the background wind into account (Karpen et al. 2012; Guidoni et al. 2016). Without a solar wind, there is no detached top of the helmet streamer, no lateral reconnection sheets form, and the expanding central arcade is not as deformed or flattened through the lateral pressure of the surrounding wind. Similar plasmoid generation is observed, but the current sheet orientation and thus the location of the magnetic island formation and the magnetic

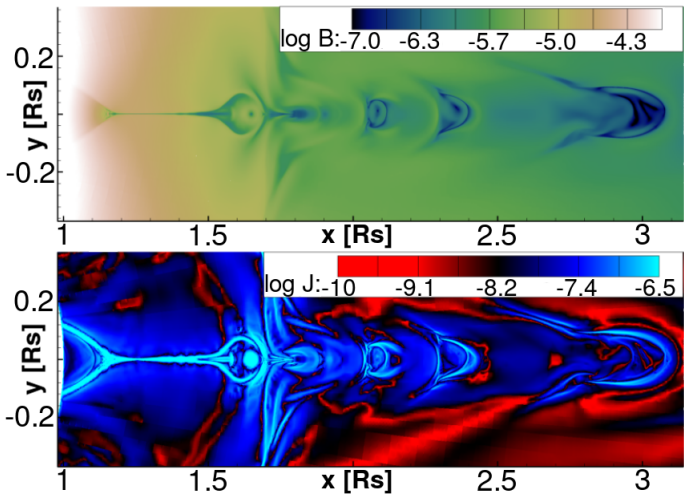

Fig. 4. Magnetic islands in the flare current sheet, shown in the *upper panel* as circular structures of magnetic field strength and in the *lower panel* as circular structures of current density (A m^{-2}), 36 h after shearing started.

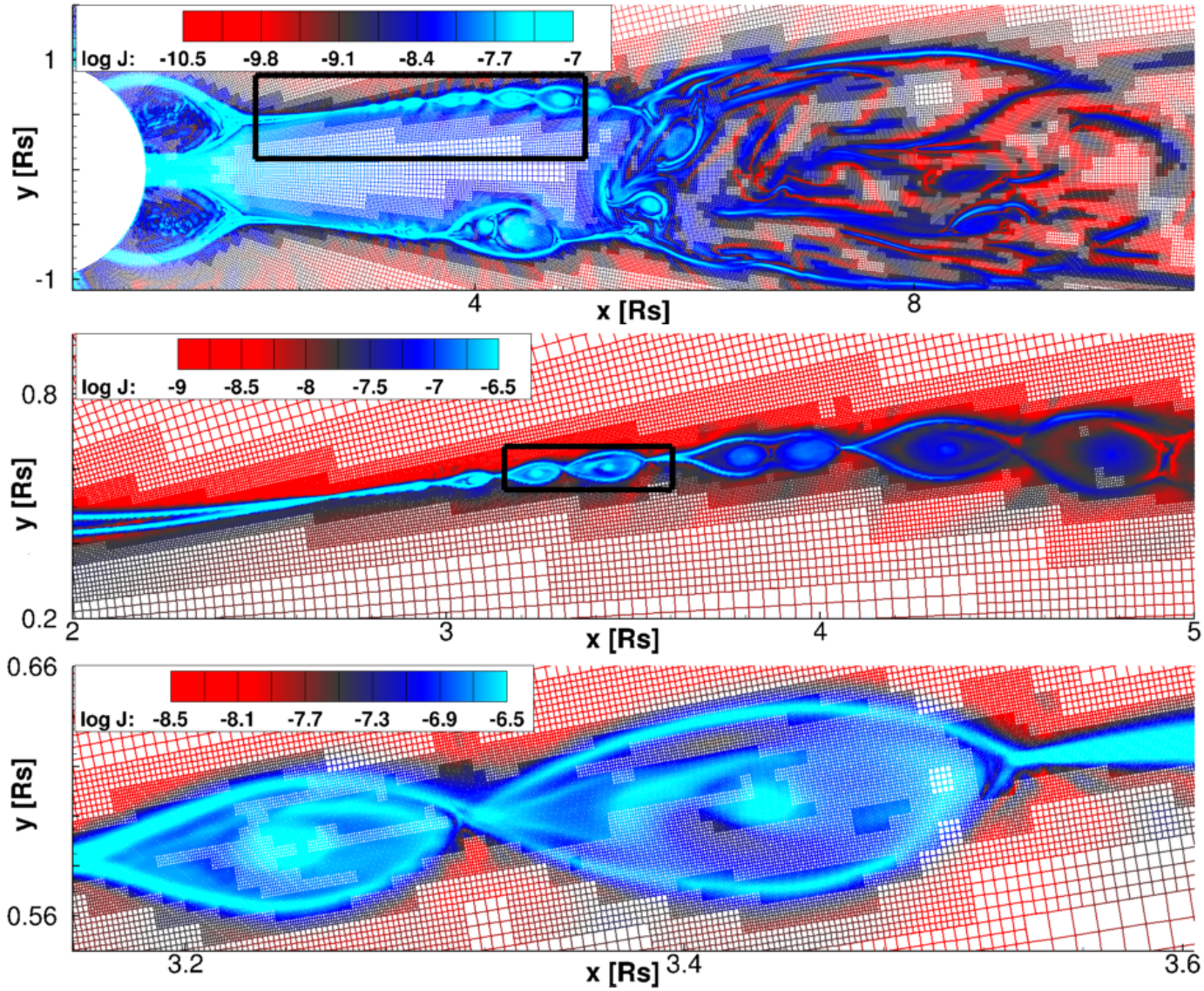

Fig. 5. Computational grid 26 h after the shearing started, where the color of the grid corresponds to the current density (A m^{-2}). Each panel down is a scaled-up plot of the region inside the black box on the figure above it. The temporal evolution of the grid can be found in Fig. A.1.

island dynamics are considerably affected by the presence of the background wind.

4.2. Resolving the current sheets with AMR

Figure 5 illustrates the effect of the AMR scheme using seven grid levels in the simulation. The image displays the final stage of the eruption; the time evolution from the start of the shearing is described in detail in the next paragraph. The figure shows only the grid in a color corresponding to the value of the current density, and each panel is a zoom-in on the black box from the panel above it. The important current-carrying structures are better resolved than the rest of the grid, with the regions of highest refinement located at the current sheets; this validates the refinement scheme.

Since the numerical resistivity (dissipation) depends on the grid resolution, the formation and dynamics of the islands should be different for the three simulations with a different number of refinement levels. This effect is clearly visible in Fig. 6, in which the same simulation is shown, but for three, five, and seven grid levels, that is, the starting (stretched) grid with two, four, and six additional refinement levels, respectively. The global picture is not affected by the numerical dissipation, and neither are the timescales. The additional refinement levels only provide more detail on the topology of the current sheets. In the upper panel, where only three grid levels are used, the two flux ropes are formed, but the resolution is too poor for any small-scale structures to be resolved. This case is very similar to the result reported by van der Holst et al. (2007), where no AMR was used. For the middle and lower panels of Fig. 6 (with five and seven grid levels, respectively), magnetic islands form in addition to the detached central arcade and top of the helmet streamer. The number and dynamics of these islands clearly depends on the numerical resolution. The reason is that the current sheets are so thin that they become plasmoid unstable, which makes island formation necessary to process the amount of reconnecting flux that the global evolution requires. With increasing resolution of a reconnection scenario, the current sheet becomes increasingly plasmoid unstable and more fine-scale structures are generated by the reconnection process. The

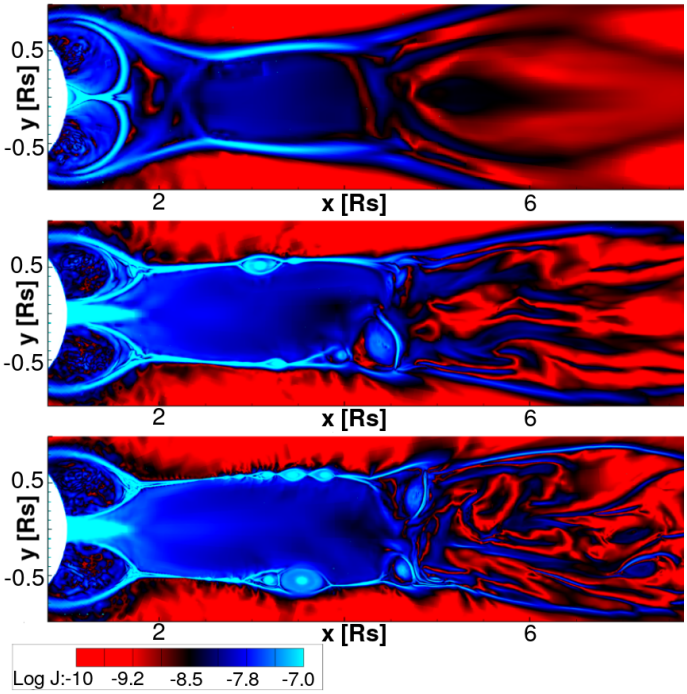

Fig. 6. Current density (A m^{-2}) at 25 h after shearing starts for three, five, and seven levels of the solution-dependent AMR (from *top* to *bottom*).

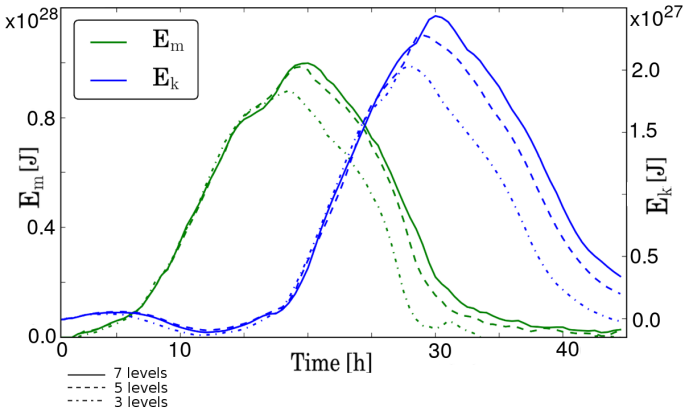

Fig. 7. Magnetic and kinetic energies where the energy of the initial state has been subtracted. The dash-dotted lines displays three grid levels, the dashed lines five levels, and the full lines seven levels.

evolution of such islands is described in detail by Guidoni et al. (2016) for the similar case without a background solar wind.

4.3. Energy evolution and dissipation in the current sheet structures

The magnetic and kinetic energy involved in the eruption, both displayed in Fig. 7, clearly show that free (non-potential) magnetic energy starts to build up as soon as the foot point shearing phase starts. The foot point shearing in the longitudinal direction creates a positive Poynting flux. The amount of free magnetic energy continues to increase until the interaction of the rising central arcade and the overlying field has created the breakout current sheet in which magnetic reconnection occurs. This process converts magnetic energy into kinetic and thermal energy. This can be seen as a strong increase in the kinetic energy, indicated by the steep blue curves in Fig. 7, which displays the evolution of the magnetic and kinetic energies of all three simulations with different maximum refinement levels. Simulations with higher resolution yield higher energy levels because the observed magnetic reconnection in the simulations is dependent on the numerical resistivity and consequently on the numerical resolution. Since the numerical resistivity is lower for higher levels of refinement, more free magnetic energy can accumulate before being converted into kinetic energy. This delays the fast reconnection process and the accompanying plasmoid formation.

It follows that the additional energy is localized in the current sheets, as Fig. 8 shows. From the top to the bottom row in this figure, the kinetic energy density is displayed for the three-, five-, and seven-grid simulations, where the left column shows the whole erupting structure 22 h after the foot point shearing started and the right column focuses on the flare current sheet in the central arcade after 32.5 h. At 22 h in the simulation, little kinetic energy is seen in either the detached helmet streamer flux structure or the erupting flux rope part of the central arcade. At this time, the high concentration of kinetic energy is found in the reconnection jet outflows of the reconnecting current sheets. Magnetic reconnection occurs in both the lateral breakout currents and the flare current sheet, although the kinetic energy in the lateral current sheets is visibly higher at this stage. At 32.5 h, the erupting structure has nearly reached the outer boundary of the computational domain. Fast flare reconnection in the flare current sheet results in a strong increase in kinetic energy in the flare current sheet. Here fast flare reconnection re-forms the closed flux streamer belt in the wake of the central arcade eruption. It is clear, however, that the magnetic reconnection process in the lateral current sheets has a much greater impact on the global energy distribution in our eruption scenario. Again the omission of the solar wind yields a very different result, where the breakout reconnection does not drive the top of the helmet streamer (since there is none in that case), and the fast magnetic reconnection at the flare current sheet is the main kinetic energy driver of the eruption.

However, Fig. 9 shows that the additional kinetic energy does not imply a higher speed of the CMEs. The upper panel reflects the velocity of the detached or erupting helmet streamer flux. Before 10 h, the central arcade expands but has not reached the X-point yet, so there is little motion of the streamer. As the central arcade then exerts more pressure against the overlying field, the helmet streamer starts to rise faster. Between $10 < t < 16.5$ h, reconnection at the breakout sheet increases as a result of the expansion of the central arcade, leading to the transition and splitting of the breakout sheet into two lateral current sheets. At approximately 16.5 h, magnetic reconnection at the lateral current sheets allows for a complete detachment of the helmet streamer top. In addition to providing more kinetic energy to drive the ejection (visible as the distinct rise of the blue curve in Fig. 7), the top of the helmet streamer is now untethered from the solar surface, resulting in a clear acceleration of the detached streamer flux structure. After approximately 26 h, the speed of the helmet streamer stabilizes before it leaves the computational domain. The lower panel of the figure shows the velocity of the central arcade. The measurements start from the moment a flux rope is formed inside the arcade, which occurs at 16.5 h. The initial rise of the arcade is decelerated because the overlying magnetic field hinders the expansion. After 20 h, the rising central arcade is subjected to less pressure because the top of the helmet streamer above it is untethered, resulting in an acceleration of the

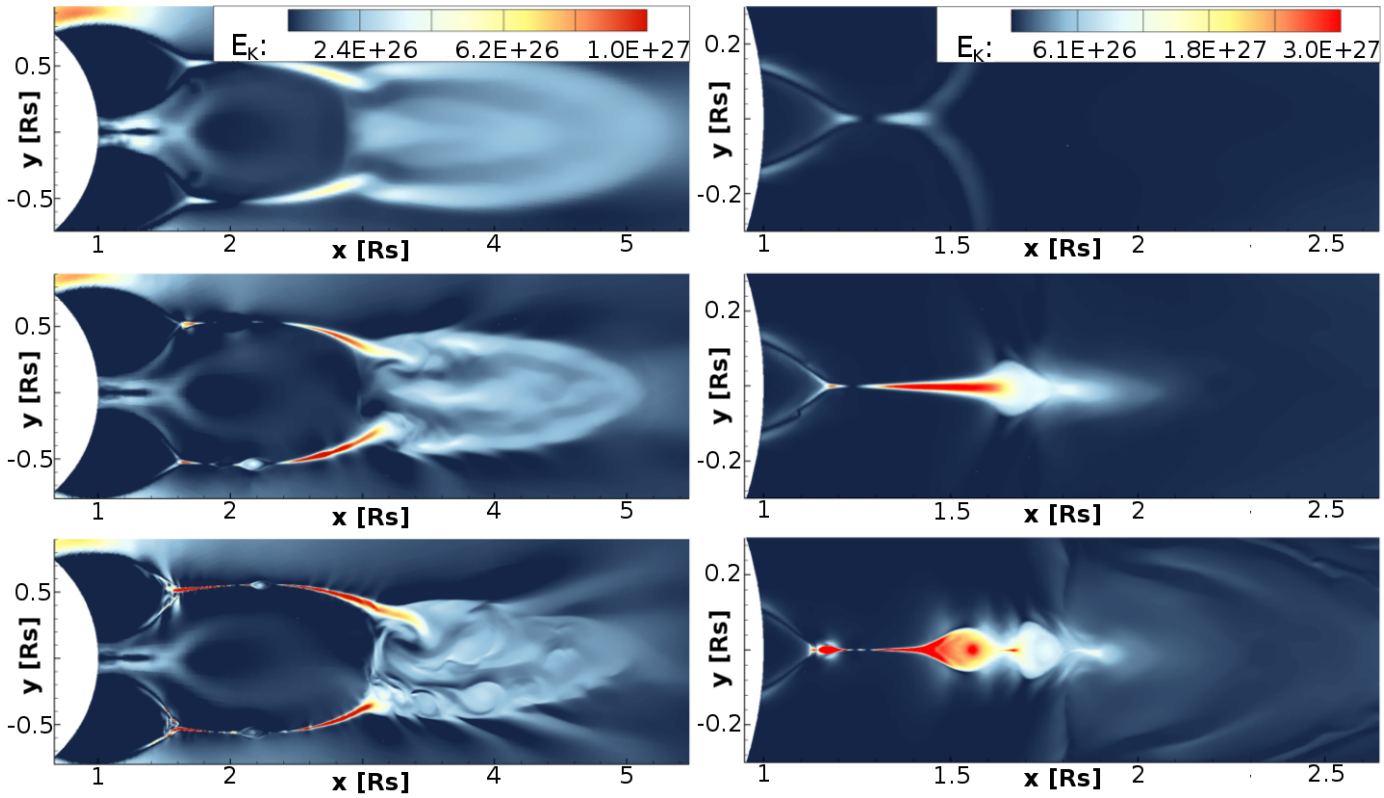

Fig. 8. Kinetic energy [J] of the CME 22 h after shearing started (*left*), and kinetic energy of the flare current sheet after 32.5 h (*right*). The *top*, *middle*, and *bottom* row show three, five, and seven grid levels, respectively.

CME. At approximately 26.5 h, fast reconnection at the flare current sheet occurs, which completely cuts the arcade loose from the solar surface. This process is barely noticeable as a small bump in the kinetic energy in Fig. 7 and a tiny increase in acceleration of the central arcade in Fig. 9. The velocities of both flux ropes stall just below 400 km s^{-1}.

5. Conclusions

We presented and discussed the results of ultrahigh-resolution numerical simulations of breakout CMEs using different levels of solution-dependent AMR. This research is a natural extension of the work of Karpen et al. (2012), which did not include a background solar wind, and that of van der Holst et al. (2007), which did not achieve the resolution required to resolve the instabilities that create the small-scale structures. The inclusion of a background wind greatly impacted the structure and dynamics of both eruption and small-scale structures that are formed during the evolution. When the background solar wind is included in the breakout CME setup, a helmet streamer structure forms around the typical triple-arcade structure. This results in a different evolution than when the background solar wind is not taken into account. The two main structural differences resulting from this inclusion are as follows: magnetic islands that form in the breakout current sheets may merge with the ejected helmet streamer, and two separate ejections occur instead of only the central arcade: the detached helmet streamer, and the pinched-off central arcade. In addition, the breakout current sheet splits up after a while into two lateral current sheets. Changing the number of grid refinement levels results in different dynamics of the magnetic islands as a result of a difference in numerical resistivities, but the global picture and timescales remain the same.

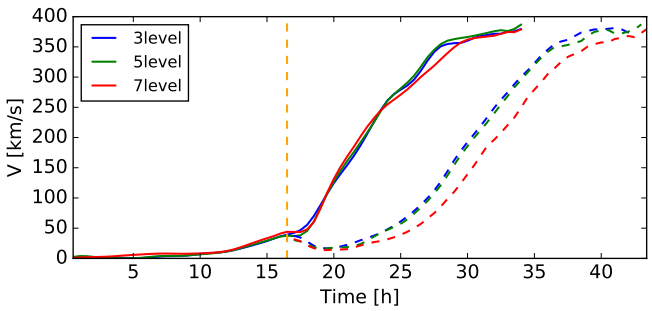

Fig. 9. Velocity plots of the two flux ropes. The full lines represent the velocity of the helmet streamer, and the dashed lines represent the velocity of the central arcade.

Furthermore, the global system energy evolution differs vastly when a background wind is taken into account. It was observed that the magnetic reconnection in the flanks of the rising central arcade is the main kinetic energy driver of the eruption, thanks to the conversion of magnetic into kinetic energy and to the force imbalance introduced by the untethering of the top of the helmet streamer, whereas without a background wind, this role is performed by the flare reconnection.

References

Allred, J. C., & MacNeice, P. J. 2015, Comput. Sci. Discovery, 8, 015002
Antiochos, S. K. 1998, ApJ, 502, L181
Antiochos, S. K., DeVore, C. R., & Klimchuk, J. A. 1999, ApJ, 510, 485
Chian, A. C.-L., & Muñoz, P. R. 2011, ApJ, 733, L34
Edmondson, J. K., Antiochos, S. K., DeVore, C. R., & Zurbuchen, T. H. 2010, ApJ, 718, 72

Eriksson, S., Newman, D. L., Lapenta, G., & Angelopoulos, V. 2014, Plasma Phys. Controlled Fusion, 56, 064008
Gopalswamy, N. 2004, in The Sun and the Heliosphere as an Integrated System, eds. G. Poletto, & S. T. Suess, Astrophys. Space Sci. Lib., 317, 201
Guidoni, S. E., DeVore, C. R., Karpen, J. T., & Lynch, B. J. 2016, ApJ, 820, 60
Jacobs, C., Poedts, S., & van der Holst, B. 2005, in Solar Wind 11/SOHO 16, Connecting Sun and Heliosphere, eds. B. Fleck, T. H. Zurbuchen, & H. Lacoste, ESA SP, 592, 641
Jacobs, C., Poedts, S., & van der Holst, B. 2006, A&A, 450, 793
Jacobs, C., van der Holst, B., & Poedts, S. 2007, A&A, 470, 359
Janvier, M. 2017, J. Plasma Phys., 83, 535830101
Karpen, J. T., Antiochos, S. K., & DeVore, C. R. 2012, ApJ, 760, 81
Khabarova, O., Zank, G. P., Li, G., et al. 2015, ApJ, 808, 181
Khabarova, O. V., Zank, G. P., Li, G., et al. 2016, ApJ, 827, 122
Leake, J. E., Linton, M. G., & Antiochos, S. K. 2014, ApJ, 787, 46
Lynch, B. J., Reinard, A. A., Mulligan, T., et al. 2011, ApJ, 740, 112
Manchester, W. B., Gombosi, T. I., Roussev, I., et al. 2004, J. Geophys. Res. (Space Phys.), 109, A02107
Porth, O., Xia, C., Hendrix, T., Moschou, S. P., & Keppens, R. 2014, ApJS, 214, 4
Riley, P., Baker, D., Liu, Y. D., et al. 2018, Space Sci. Rev., 214, 21
Singh, A. K., Siingh, D., & Singh, R. P. 2010, Surv. Geophys., 31, 581
Smolyakov, A. I., Hirose, A., Lazzaro, E., Re, G. B., & Callen, J. D. 1995, Phys. Plasmas, 2, 1581
Steinolfson, R. S. 1991, ApJ, 382, 677
van der Holst, B., Poedts, S., Chané, E., et al. 2005, Space Sci. Rev., 121, 91
van der Holst, B., Jacobs, C., & Poedts, S. 2007, ApJ, 671, L77
Xia, C., Teunissen, J., El Mellah, I., Chané, E., & Keppens, R. 2018, ApJS, 234, 30
Zhao, K. J., Shi, Y. J., Hahn, S. H., et al. 2015, Nucl. Fusion, 55, 073022
Zuccarello, F. P., Jacobs, C., Soenen, A., et al. 2009, A&A, 507, 441

Appendix A: Temporal evolution

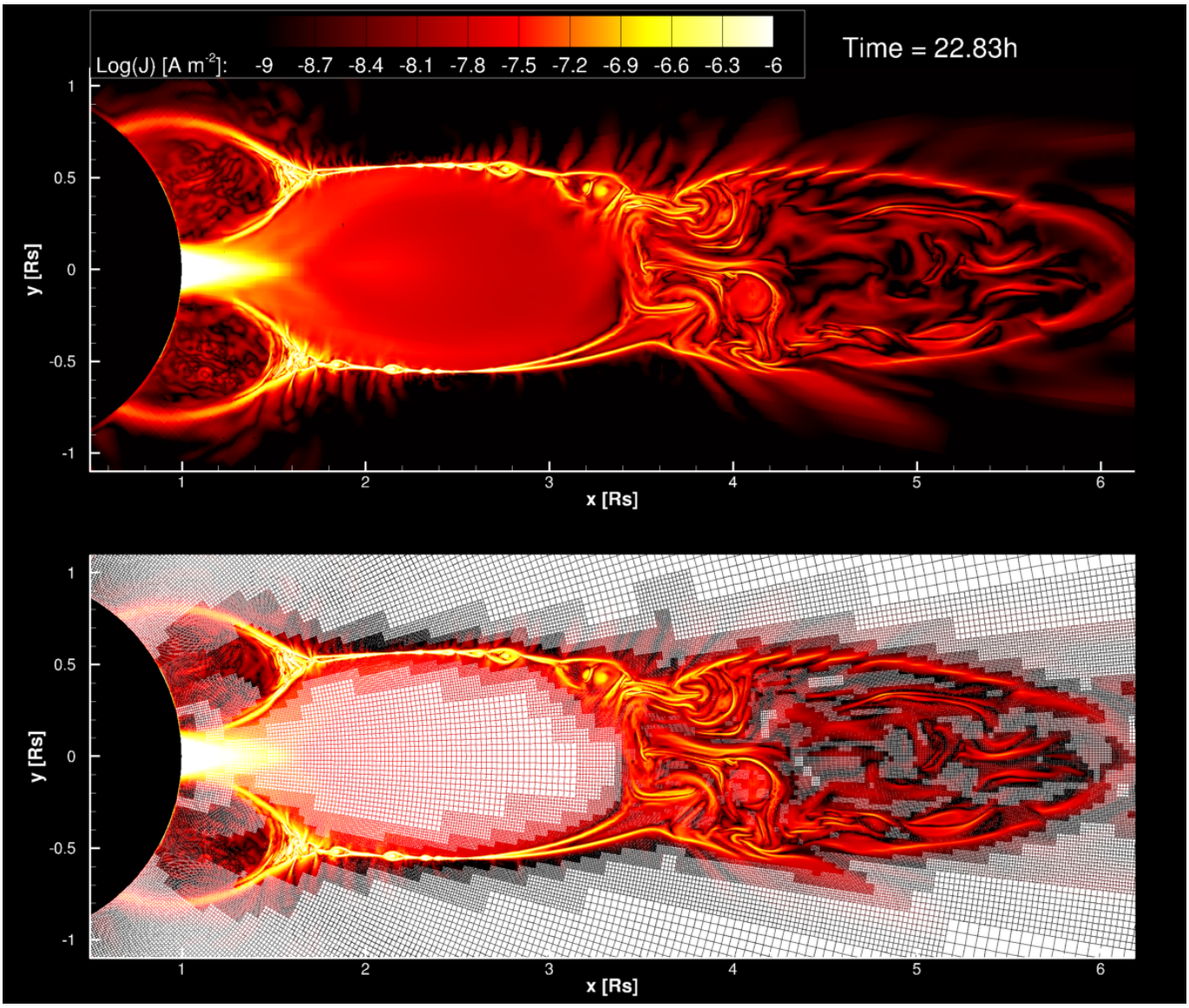

Fig. A.1. *Upper panel*: current density. *Lower panel*: grid colored to the current density (similar to Fig. 5). A movie of the temporal evolution is available online.